



Time-frequency analysis of nonlinear terahertz signals due to hot electrons in the nonparabolic conduction bands of n -doped $\text{In}_{0.57}\text{Ga}_{0.43}\text{As}$ films

C. M. Garcia-Rosas ¹, X. Chai,¹ X. Ropagnol,^{1,2} and T. Ozaki^{1,*}

¹*Institut National de la Recherche Scientifique–Énergie Matériaux Télécommunications, 1650 boulevard Lionel Boulet, Varennes, Québec, Canada J3X 1S2*

²*Electrical Engineering Department, École de Technologie Supérieure (ÉTS), 1100 rue Notre-Dame Ouest, Montréal, Québec, Canada H3C 1K3*

 (Received 25 January 2021; revised 5 August 2021; accepted 20 September 2021; published 4 October 2021)

In this Research Letter, we study the transient carrier dynamics and the nonlinear terahertz effects induced by an intense multicycle terahertz pulse in the n -doped semiconductor $\text{In}_{0.57}\text{Ga}_{0.43}\text{As}$. For incident terahertz pulses with relatively high frequency ≥ 1 THz, we reveal the generation of low- and high-frequency components in the transmitted intensity spectra. We study the time emission of these components at different frequencies using the Gábor transform, showing that the low- and high-frequency components are due to the nonparabolicity of the conduction band. Our results demonstrate that for a multicycle terahertz pulse, we generate a distorted biphasic truncated exponential current with the driving terahertz fields, leading to discrete high-order harmonic generation in the transmitted intensity spectra.

DOI: [10.1103/PhysRevB.104.L161201](https://doi.org/10.1103/PhysRevB.104.L161201)

I. INTRODUCTION

Owing to the rapid advancements in intense terahertz (THz) radiation sources, there have recently been significant breakthroughs in our understanding of intense THz-matter interactions and nonlinear THz effects [1–7]. For example, several theoretical and experimental studies have shown efficient THz frequency multiplication, such as high-order sideband generation (HSG) [8,9] and high-order THz harmonic generation [8–15] using intense multicycle THz pulses transmitted through various materials. These materials include bulk crystals, such as gallium selenide (interpreted via dynamical Bloch oscillations) [13,14], tungsten diselenide (modeled by THz-driven electron-hole collisions) [8,9], and graphene (explained via the interplay between the interband and intraband motion of the carriers and hot Dirac fermion dynamics) [10–12,15]. Using a 100-fs near-infrared excitation pulse and a high-intensity THz pulse with MV/cm peak electric fields, Langer *et al.* have observed in WSe_2 that the recolliding electrons and holes emit light via multiple HSG [8,9]. Moreover, Hafez and co-workers have reported the generation of THz harmonics in a single layer of graphene, driven by multicycle intense THz pulses with peak field strengths of only $\sim 10^{-1}$ – 10^3 kV/cm [11,15]. Nevertheless, as we have seen in the visible and near-infrared regimes, nonlinear effects give rise to a multitude of fascinating phenomena, many of which could still be hiding in experimental data.

To further deepen our understanding of nonlinear THz effects, we perform in this Research Letter a systematic time-frequency study of the response of a classical n -doped semiconductor $\text{In}_{0.57}\text{Ga}_{0.43}\text{As}$ thin film when pumped by a

multicycle THz pulse with central frequencies from 0.2 to 1.5 THz and incident peak electric fields ranging from 100 up to 500 kV/cm. We show that high-order harmonic generation (HHG) is strongly dependent not only on the peak field strength but also on the central frequency of the incoming pulse. Indeed, we put in evidence that HHG is mainly generated by intervalley scattering. By applying the Gábor transform formalism [16–18], we also show that the emission due to HHG starts only when the photocurrent has a distorted biphasic truncated exponential form, which is evident for low THz frequency. On the other hand, HHG for higher THz frequencies is not as prominent because the necessary time for inducing the truncation of current generated by the THz pulse becomes comparable to the duration of the half cycle of the THz pulse. In addition to HHG, we observe the generation of spectral components above and below the fundamental wave. We refer to these waves, which are in higher and lower frequencies than the central frequency of the main pulse, as high-frequency components (HFCs) and low-frequency components (LFCs). We use a time-frequency analysis based on the Gábor transform to study the transmitted electric field, putting in evidence that these HFCs and LFCs are generated only through intravalley scattering effects. It is important to note that similar LFCs and HFCs besides the fundamental frequency have been observed in recent reports on intense THz-matter interactions, such as those detected in the high-order harmonic spectra from graphene [11,15]. Given that nonparabolicity of the conduction band is the cause for these LFCs and HFCs, we expect them to be generated in many semiconductors (including graphene), potentially providing a method to experimentally study their band structure.

II. THEORY

To understand the nonlinear carrier dynamics and the wave generation induced by the response of the InGaAs

*Author to whom correspondence should be addressed: Tsuneyuki.Ozaki@inrs.ca

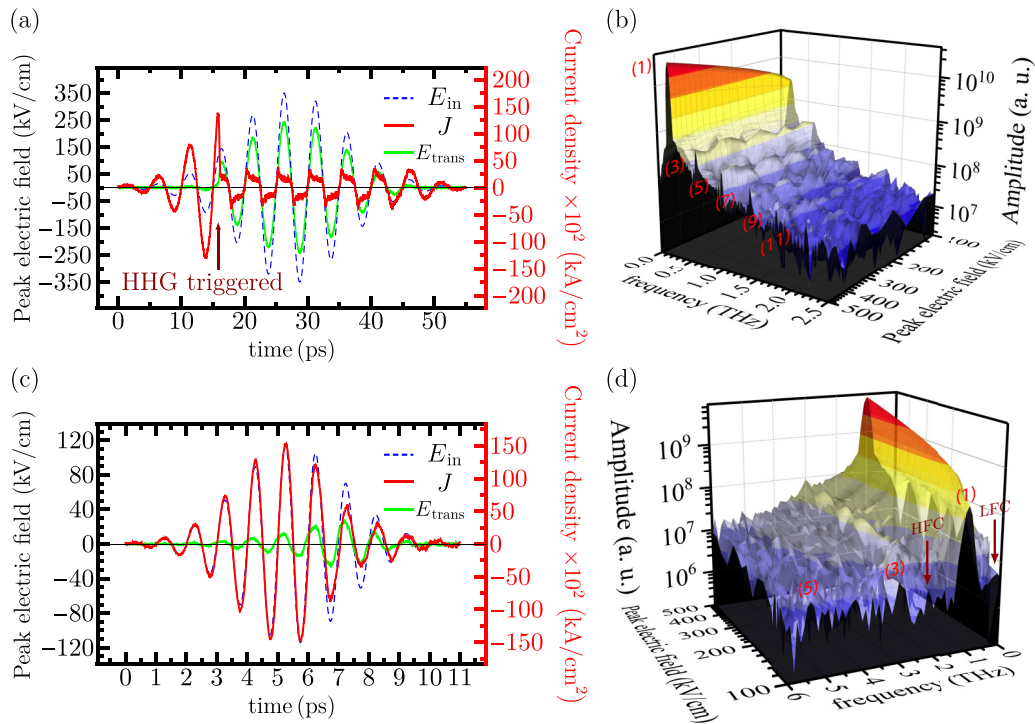


FIG. 1. Current density (red solid line) and transmitted THz wave form (lime green solid line) generated by a multicycle THz pulse (blue dashed line) centered at (a) 0.2 THz and (c) 1.0 THz. The incident peak fields used here are (a) 350 kV/cm for the 0.2-THz pulse and (c) 114 kV/cm for the 1.0-THz pulse. Amplitude spectra of the transmitted THz wave forms as a function of the THz peak electric fields, for fundamental frequencies of (b) 0.2 THz and (d) 1.0 THz.

layer to multicycle THz pulses, we performed a theoretical analysis in the time domain by using the thin-film equation [5,7,12,19], considering that the sample could be idealized as a thin conducting sheet with thickness d on an insulating substrate with refractive index N [5]. In our study, the sample is a 500-nm-thick n -type $\text{In}_{0.57}\text{Ga}_{0.43}\text{As}$ (100) epilayer with a doping concentration of $2 \times 10^{18} \text{ cm}^{-3}$ [7]. If the THz pulse irradiates the sample from the InP substrate side (substrate/thin-film/air configuration) [20], the thin-film equation is given by the expression

$$E_{\text{trans}}(t) = \frac{1}{Y_0 + Y_S} \left[\frac{4Y_S}{N+1} E_{\text{in}}(t) - J(t)d \right]. \quad (1)$$

Here, $E_{\text{trans}}(t)$ and $E_{\text{in}}(t)$ are the transmitted and incident THz fields, respectively, $Y_0 = (377 \Omega)^{-1}$ is the free-space admittance, and $Y_S = NY_0$ is the admittance of the substrate, in which $N = 3.1$ is the refractive index of InP at THz frequencies [19]. We implement an analytical-band ensemble Monte Carlo approach to solve the Boltzmann transport equation [21–24] for modeling the transient carrier dynamics of the sample, as previously employed in Ref. [6]. To detail the different scattering effects in our simulations, we consider the typical scattering mechanism in a compound semiconductor such as acoustic, Coulomb, and polar optical phonon scattering, as well as intravalley and intervalley scattering [21,25]. Through these simulations, we obtain the carrier dynamics in the Γ , L , and X valleys of the conduction band, and the current density $J(t)$ was directly determined by the average drift velocity [12,26–28].

III. RESULTS

We first performed simulations on the nonlinear THz effects induced by intense multicycle THz radiation in n -doped $\text{In}_{0.57}\text{Ga}_{0.43}\text{As}$. In the simulations, we consider a temperature of 300 K and use the physical constants of the $\text{In}_{0.57}\text{Ga}_{0.43}\text{As}$ sample reported by Long *et al.* [23] and Razzari *et al.* [4].

A. THz pulses with relatively low and high frequency

Figure 1 shows the incident and transmitted THz wave form for THz pulses with central frequencies of 0.2 and 1.0 THz. The incident peak electric fields used here are 350 kV/cm for the 0.2-THz pulse and 114 kV/cm for the 1.0-THz pulse. For THz pulses with 0.2 and 0.4 THz, we found that the distorted current density shows a sharp truncation {see Fig. 1(a) and also Fig. S2(a) of the Supplemental Material (SM) [29]}. On the other hand, for the THz pulses with 1.0 and 1.5 THz, it is challenging to observe clear current truncations faster than the duration of the half cycle of the original incident THz wave form {see Fig. 1(c) and also Fig. S2(c) of the SM [29]}.

For relatively low frequency multicycle pulses and high incident peak fields, the direct consequence of the distorted current phases with the driving THz fields is the clear high-order harmonic (HH) peaks in the transmitted intensity spectra (up to the eleventh and seventh harmonic for 0.2- and 0.4-THz pulses, respectively) {see Fig. 1(b) and also Fig. S2(b) of the SM [29]}. In contrast, for relatively high frequency and

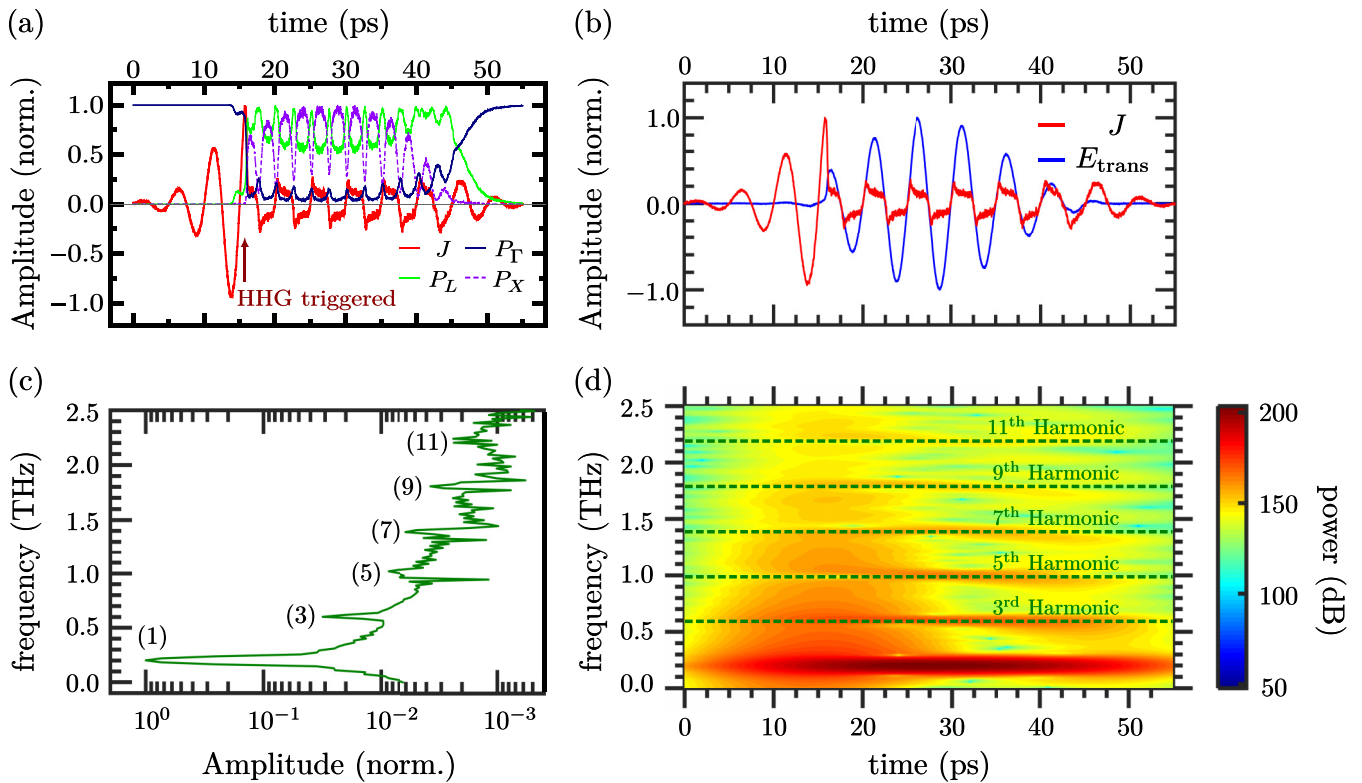


FIG. 2. Time-frequency analysis, or Gábor transform for the incident peak fields at 350 kV/cm for a 0.2-THz pulse. (a) Normalized (norm.) temporal current density (solid red line), and carrier populations in the Γ (dark blue solid line), L (lime green solid line), and X (dashed violet line) valleys. (b) Current density (red solid line) and transmitted multicycle THz pulse (blue solid line). (c) The corresponding transmitted amplitude spectra. (d) HHs (dashed green lines) are shown during the time of the pulse.

low incident peak fields, the changes in the frequency are not so clear to observe due to the absence of clear current truncations. However, we can still barely observe HHG in the intensity spectra (up to the fifth order when pumped by the 1.0-THz pulses and up to the third order when pumped by the 1.5-THz pulses) [see Fig. 1(d) and also Fig. S2(d) of the SM [29]]. In addition, we can also observe some small peaks that are located at 0.3 and 1.7 THz when the sample is pumped by the 1.0-THz pulses. These frequencies, which do not correspond to any harmonic order, are LFCs and HFCs [see Fig. 3(c)].

For an ideal square wave, the harmonic order of the Fourier decomposition would extend to infinity. In our case, the intensity and order of the HHG depend on the modulation of the photocurrent; the stronger and faster are the truncations of the photocurrent, the higher are the HHs' orders. As a result, the HHG is easier to observe using a relatively low frequency source, resulting in a better temporal truncation contrast of the current density due to the drastic change of the carrier population in the satellite valleys [see Fig. 1(b)]. Moreover, for relatively high frequency THz pulses at similar field strengths, it is difficult to have sharper truncations, and therefore the harmonics [such as the fifth harmonic of the 1.0-THz pulse in Fig. 1(d)] are less evident. However, under these conditions, we observe frequencies located just above and below the fundamental frequency of the main pulse. These HFCs and LFCs are evident when we pump the InGaAs thin film with relatively high frequency multicycle THz pulses. Surprisingly, the HHG intensity decreases by increasing the

intensity of the pump pulse, and the LFCs and HFCs vanish [see Fig. 1(d) and also Figs. S2(d) and S7 of the SM [29]].

To measure with accuracy in both the time and frequency domains, we performed a time-frequency analysis, which allows us to capture the entire time-frequency content of the transmitted multicycle THz wave forms and at the same time generate a spectrogram [16,17]. For this, we applied the Gábor transform formalism to the transmitted multicycle THz wave forms to explain and understand the HHG, LFCs, and HFCs exhibited at different frequencies of the spectra [18].

B. Time-frequency analysis for low-frequency THz pulses

First, to better understand the HHG from relatively low frequency multicycle THz pulses (0.2 THz) and high incident peak field (350 kV/cm), we analyze the carrier populations in the Γ , L , and X valleys. Figure 2(a) shows a drastic reduction in the carrier population of the Γ valley around 16 ps. At that moment, because of the high incident field, the ponderomotive acceleration is strong enough that the carriers gain sufficient kinetic energy to efficiently undergo intervalley scattering from the Γ to the L and X valleys [7]. The HHG is mainly caused by the intervalley transitions of the carriers from the Γ valley to the L and X valleys, and also from L valleys to X valleys and vice versa. This process of intervalley scattering between the Γ valley and the satellite valleys is repeated or continued throughout the THz pulse. Furthermore, the time-frequency analysis shows that the third harmonic is emitted around the highest intensity and the fifth and higher

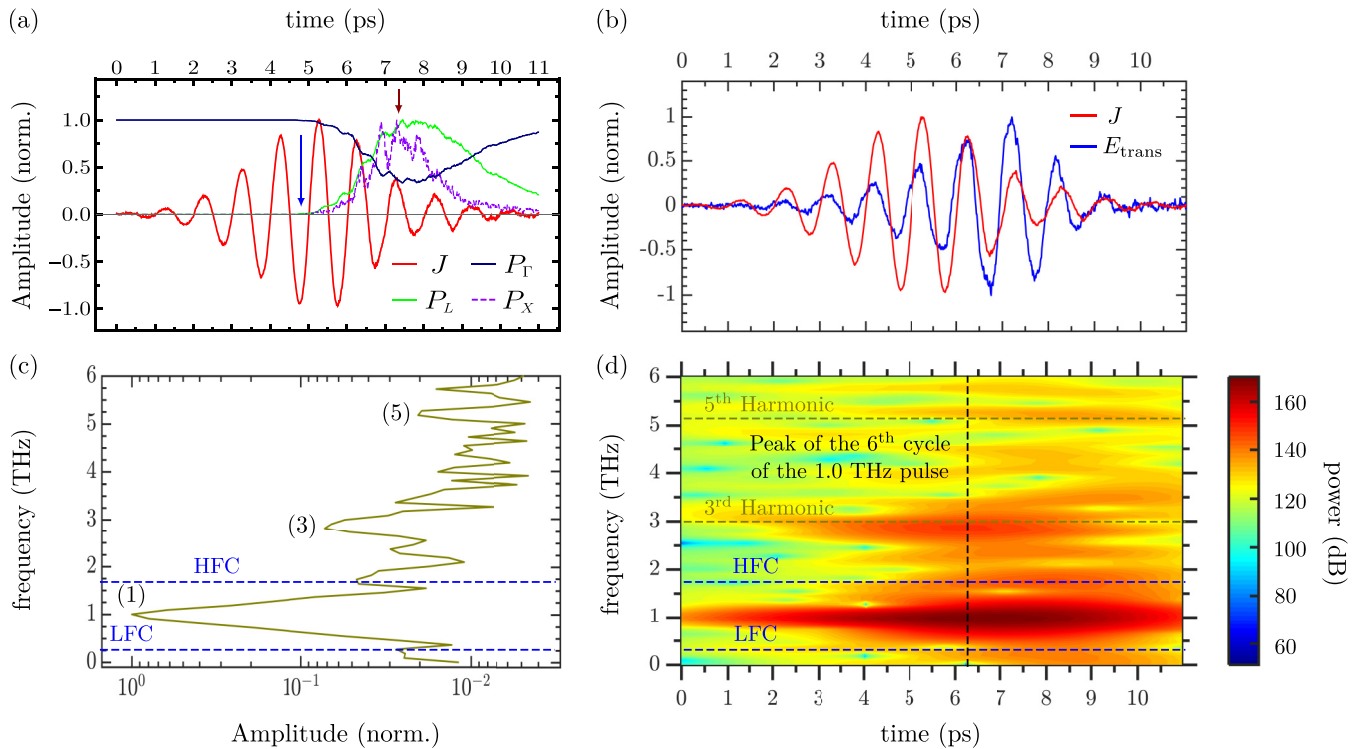


FIG. 3. Time-frequency analysis, or Gábor transform for the incident peak fields at 114 kV/cm for a 1.0-THz pulse. (a) Normalized temporal current density (solid red line), and carrier populations in the Γ (dark blue solid line), L (lime green solid line), and X (dashed violet line) valleys. (b) Current density (red solid line) and transmitted multicycle THz pulse (blue solid line). (c) The corresponding transmitted amplitude spectra. (d) HHs (dashed olive green lines) are emitted throughout the THz pulse, and for the LFCs and HFCs the emission is observed after the time when the peak of the fourth cycle in the 1.0-THz pulse arrives, while their emission is much lower for earlier times.

harmonics only appear at certain times of the THz pulse and with weaker intensity [see Fig. 2(d)] because as we strongly reduce the number of contributing recombination times, only the high frequencies near the cutoff frequency $\omega_{\text{cut}}^{\text{HHG}}$ become enhanced [30].

C. Time-frequency analysis for high-frequency THz pulses

Next, we compute the carrier population for the 1.0-THz pulse with an incident peak field at 114 kV/cm. Up until the peak of the fourth cycle of the current density [see blue arrow in Fig. 3(a)], the carriers remain in the Γ valley, but after a few picoseconds, the electrons gain enough energy to be scattered from the Γ valley to the higher satellite valleys. However, we can clearly see that the maximum intensity of the third harmonic is occurring at the same time as the maximum intensity of the THz pulse, precisely when the carrier populations of the L and X valleys achieve a maximum [see the red arrow in Fig. 3(a)]. If we look at the LFCs (0.3 THz) and HFCs (1.7 THz), considerably strong emission compared with the HH peaks is observed a few picoseconds after the peak of the sixth cycle of the current density.

We perform additional calculations for the case of relatively high THz frequency and low incident peak field. For a peak electric field of 100 kV/cm, (i) the change in the carrier population in the Γ valley is small, (ii) low-frequency components appear in the transmitted amplitude spectra, and (iii) high-order harmonics become apparent but with very low intensity. When we increase the peak electric field, the

high-frequency components become evident when the peak electric fields are 110–125 kV/cm [see Fig. S7 of the SM [29]]. The nonlinear effect starts to become complex over 140 kV/cm because the carrier population of the X and L valleys begins to increase rapidly within the duration of the THz pulse, and the scattering time is suddenly reduced. Hence, for the higher incident peak field, the HHG has a weak intensity, and the LFCs and HFCs vanish. These results show a strong correlation between the carrier population in the Γ valley and the nonlinear THz emission in both low- and high-frequency components. This confirms that for nonlinear THz effects to occur, we need a sufficient population of carriers in the Γ valley. Also, the emission of the LFCs and HFCs does not span the whole duration of the THz pulse for 110–125 kV/cm peak fields because having both effects at the same time may decrease the efficiency of both processes.

D. Average effective carrier mass

Next, we apply the fast Fourier transform (FFT) to the calculated average carrier effective mass $\langle m_i^* \rangle$ (for each $i = \Gamma, L, \text{ and } X$ valleys) to observe the variation of $\langle m_i^* \rangle$ with time when it is irradiated by a THz field and associate the frequency components that result in the amplitude spectra of $\langle m_i^* \rangle$ with the odd harmonics of the 0.2- and 1.0-THz pulses. When the electric field of the THz pulse is weak, $\langle m_i^* \rangle$ is constant, and thus nonlinear THz effects are not observed in the current density and transmitted THz pulse. In this case, the amplitude

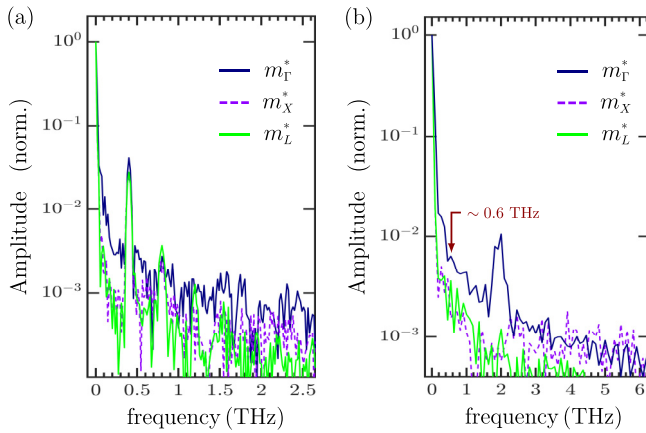


FIG. 4. Amplitude spectra of each average carrier effective mass for the incident peak fields at (a) 350 kV/cm for 0.2 THz and (b) 114 kV/cm for 1.0 THz.

spectrum of $\langle m_i^* \rangle$ will be a narrow function centered at 0 THz, and the current density oscillates at the driving THz frequency. However, when the THz field is increased [see Fig. S6 of the SM [29]], we find several peaks appearing in the amplitude spectra of $\langle m_i^* \rangle$ [see Fig. 4] and, as a consequence, a distorted biphasic truncated exponential current density [see Fig. 1(a)]. The most prominent peaks that appear in the amplitude spectra of $\langle m_i^* \rangle$ are those that result in the harmonic generation of the incident THz pulse. For example, in Fig. 4(b), the peak centered at 2 THz in the amplitude spectra of $\langle m_i^* \rangle$ results in the third harmonic of the 1.0-THz pulse because $\langle m_i^* \rangle$ has a $2\omega_{\text{THz}}$ component; hence the current density is modulated by $2\omega_{\text{THz}}$, and it will have a $3\omega_{\text{THz}}$ component (this is $\omega_{\text{THz}} + 2\omega_{\text{THz}}$). This modulation in $\langle m_i^* \rangle$ results in modulations in $J(t)$, thus generating the harmonics via intervalley scattering. Moreover, under the same criteria, the peaks at ~ 0.4 , ~ 0.8 , ~ 1.2 , ~ 1.6 , and ~ 2.0 THz in Fig. 4(a) result in the odd harmonics of the 0.2-THz pulse, because $\langle m_i^* \rangle$ has $0.4\omega_{\text{THz}}$, $0.8\omega_{\text{THz}}$, $1.2\omega_{\text{THz}}$, $1.6\omega_{\text{THz}}$, and $2.0\omega_{\text{THz}}$ components, and thus the current density will have $0.6\omega_{\text{THz}}$, $1.0\omega_{\text{THz}}$, $1.4\omega_{\text{THz}}$, $1.8\omega_{\text{THz}}$, and $2.2\omega_{\text{THz}}$ components. However, we find another peak in the amplitude spectra of $\langle m_i^* \rangle$ of the 1.0-THz pulse centered at ~ 0.6 THz [see Fig. 4(b)]. If the current density is modulated by $a\omega_{\text{THz}}$, where for this case $a < 1$, then it will have $(1 \pm a)\omega_{\text{THz}}$ components, which are the low- and high-frequency components located at ~ 0.4 and ~ 1.6 THz, respectively, shown in Fig. 3(c). We have to note that since these two peaks are broad, and due to the complicated tem-

poral emission and structures, the central frequencies of the HFCs and LFCs do not perfectly match. It is important to note that whereas THz high-order harmonics are generated by both intervalley and intravalley effects, the LFCs and HFCs are purely intravalley effects, reflecting the nonparabolicity of the conduction band.

IV. SUMMARY

Our results show that, for relatively low frequency multi-cycle THz pulses and high incident peak fields, the carriers are accelerated to high average energy and the truncation in the current density is first achieved (leading to discrete HHG). The LFC and HFC generation that appears in the transmitted amplitude spectra is due to carriers in the Γ valley accelerated to high energies, thus decreasing their mobility, causing the generated current to oscillate at lower and higher frequencies. This effect disappears at higher THz intensities since the carriers are quickly scattered into adjacent valleys [see Fig. 1(d) and also Fig. S2(d) of the SM [29]]. Furthermore, for relatively high frequency pulses and low fields, the intervalley scattering does not result in clear harmonics due to the temporal contrast. In addition, the current density will be large in this case, which can result in a huge emitted field along the entire THz wave form. It has to be noticed that LFCs and HFCs should be also present when the InGaAs thin film is pumped with a multi-cycle THz pulse with central frequencies of 0.2 and 0.4 THz. However, since the main scattering mechanism of the carriers at these particular low frequencies is intervalley scattering, the intravalley scattering is much weaker, disabling its clear observation in the transmitted spectra. Moreover, by using the Gábor transform, we have clarified the time of emission of photons at different frequencies, providing a better understanding of the carrier dynamics. Finally, this work serves as a guideline for experiments using other possible doped semiconductors, as well as graphene [11,15]. Moreover, our findings show that the generation of LFCs and HFCs is possible in InGaAs, but since these components are much weaker than the main THz pulse, they will require measurements with higher signal-to-noise ratio to be identified.

ACKNOWLEDGMENTS

This work was supported by the Natural Sciences and Engineering Research Council of Canada (NSERC). C.M.G. R. acknowledges the scholarship and financial support from MITACS: Globalink Graduate Fellowship Program. We thank F. Blanchard for insightful discussions and comments on the manuscript.

[1] S. Ni, S. Chai, S. S. Wu, P. F. Cui, J. Yu, and S. L. Cong, *Chem. Phys. (Washington, DC)* **534**, 110749 (2020).
 [2] O. V. Chefonov, A. V. Ovchinnikov, S. A. Romashevskiy, X. Chai, T. Ozaki, A. B. Savel'ev, M. B. Agranat, and V. E. Fortov, *Opt. Lett.* **42**, 4889 (2017).
 [3] P. Salén, M. Basini, S. Bonetti, J. Hebling, M. Krasilnikov, A. Y. Nikitin, G. Shamuilov, Z. Tibai, V.

Zhaunerchyk, and V. Goryashko, *Phys. Rep.* **836–837**, 1 (2019).

[4] L. Razzari, F. H. Su, G. Sharma, F. Blanchard, A. Ayesheshim, H. C. Bandulet, R. Morandotti, J. C. Kieffer, T. Ozaki, M. Reid, and F. A. Hegmann, *Phys. Rev. B* **79**, 193204 (2009).
 [5] G. Sharma, L. Razzari, F. H. Su, F. Blanchard, A. Ayesheshim, T. L. Cocker, L. V. Titova, H. C. Bandulet, T. Ozaki, J. C.

- Kieffer, R. Morandotti, M. Reid, and F. A. Hegmann, *IEEE Photonics J.* **2**, 578 (2010).
- [6] X. Chai, X. Ropagnol, A. Ovchinnikov, O. Chefonov, A. Ushakov, C. M. Garcia-Rosas, E. Isgandarov, M. Agranat, T. Ozaki, and A. Savel'ev, *Opt. Lett.* **43**, 5463 (2018).
- [7] X. Chai, X. Ropagnol, S. M. Raeis-Zadeh, M. Reid, S. Safavi-Naeini, and T. Ozaki, *Phys. Rev. Lett.* **121**, 143901 (2018).
- [8] F. Langer, M. Hohenleutner, C. P. Schmid, C. Poellmann, P. Nagler, T. Korn, C. Schüller, M. S. Sherwin, U. Huttner, J. T. Steiner, S. W. Koch, M. Kira, and R. Huber, *Nature (London)* **533**, 225 (2016).
- [9] F. Langer, C. P. Schmid, S. Schlauderer, J. F. M. Gmitra, P. Nagler, C. Schüller, T. Korn, P. G. Hawkins, J. T. Steiner, U. Huttner, S. W. Koch, M. Kira, and R. Huber, *Nature (London)* **557**, 76 (2018).
- [10] I. Al-Naib, J. E. Sipe, and M. M. Dignam, *Phys. Rev. B* **90**, 245423 (2014).
- [11] H. A. Hafez, S. Kovalev, J. C. Deinert, Z. Mics, B. Green, N. Awari, M. Chen, S. Germanskiy, U. Lehnert, J. Teichert, Z. Wang, K. J. Tielrooij, Z. Liu, Z. Chen, A. Naritaa, K. Müllen, M. Bonn, M. Gensch, and D. Turchinovich, *Nature (London)* **561**, 507 (2018).
- [12] P. Bowlan, E. Martinez-Moreno, K. Reimann, T. Elsaesser, and M. Woerner, *Phys. Rev. B* **89**, 041408(R) (2014).
- [13] O. Schubert, M. Hohenleutner, F. Langer, B. Urbanek, C. Lange, U. Huttner, D. Golde, T. Meier, M. Kira, S. W. Koch, and R. Huber, *Nat. Photonics* **8**, 119 (2014).
- [14] F. Langer, S. Baierl, U. Huttner, S. W. Koch, M. Kira, M. A. Huber, F. Mooshammer, M. Plankl, D. Peller, T. L. Cocker, J. Repp, and R. Huber, in *Nonlinear Optics* (Optical Society of America, Washington, DC, 2017), p. NW2A.5.
- [15] S. Kovalev, H. A. Hafez, K.-J. Tielrooij, J.-C. Deinert, I. Ilyakov, N. Awari, D. Alcaraz, K. Soundarapandian, D. Saleta, S. Germanskiy, M. Chen, M. Bawatna, B. Green, F. H. L. Koppens, M. Mittendorff, M. Bonn, M. Gensch, and D. Turchinovich, *Sci. Adv.* **7**, eabf9809 (2021).
- [16] J. N. Kutz, *Data-Driven Modeling and Scientific Computation: Methods for Complex Systems and Big Data*, 1st ed. (Oxford University Press, New York, 2013).
- [17] S. Mallat, *A Wavelet Tour of Signal Processing: The Sparse Way*, 3rd ed. (Academic, Orlando, 2008).
- [18] I. Tikhomirov, T. Sato, and K. L. Ishikawa, *Phys. Rev. Lett.* **118**, 203202 (2017).
- [19] F. Blanchard, D. Golde, F. H. Su, L. Razzari, G. Sharma, R. Morandotti, T. Ozaki, M. Reid, M. Kira, S. W. Koch, and F. A. Hegmann, *Phys. Rev. Lett.* **107**, 107401 (2011).
- [20] A. T. Tarekegne, K. Iwaszczuk, M. Zalkovskij, A. C. Strikwerda, and P. U. Jepsen, *New J. Phys.* **17**, 043002 (2015).
- [21] C. Jacoboni and L. Reggiani, *Rev. Mod. Phys.* **55**, 645 (1983).
- [22] D. Vasileska and S. M. Goodnick, *Mater. Sci. Eng., R* **38**, 181 (2002).
- [23] A. P. Long, P. H. Beton, and M. J. Kelly, *J. Appl. Phys. (Melville, NY)* **62**, 1842 (1987).
- [24] M. Mohamed, A. Bharthuar, and U. Ravaioli (2015), DOI:10.4231/D38C9R505.
- [25] M. Lundstrom, *Fundamentals of Carrier Transport*, 2nd ed. (Cambridge University Press, Cambridge, 2000).
- [26] W. Kuehn, P. Gaal, K. Reimann, M. Woerner, T. Elsaesser, and R. Hey, *Phys. Rev. B* **82**, 075204 (2010).
- [27] K. Reimann, *Rep. Prog. Phys.* **70**, 1597 (2007).
- [28] W. Kuehn, P. Gaal, K. Reimann, M. Woerner, T. Elsaesser, and R. Hey, *Phys. Rev. Lett.* **104**, 146602 (2010).
- [29] See Supplemental Material at <http://link.aps.org/supplemental/10.1103/PhysRevB.104.L161201> which includes Refs. [7,16,17,20,23,26,28,31–37], for a discussion of the carrier dynamics in the nonparabolic conduction band, the carrier transport in multivalley semiconductors, and the calculation of the average effective mass of carriers. Here, we also include the simulations of HHG, LFCs, and HFCs for 0.4- and 1.5-THz pulses, the Gábor transform analysis of other THz pulses with HHG, LFCs, and HFCs, and the evolution of the LFCs and HFCs.
- [30] I. Floss, C. Lemell, G. Wachter, V. Smejkal, S. A. Sato, X. M. Tong, K. Yabana, and J. Burgdörfer, *Phys. Rev. A* **97**, 011401(R) (2018).
- [31] E. O. Kane, *J. Phys. Chem. Solids* **1**, 249 (1957).
- [32] L. D. Whalley, J. M. Frost, B. J. Morgan, and A. Walsh, *Phys. Rev. B* **99**, 085207 (2019).
- [33] V. A. Altschul, A. Fraenkel, and E. Finkman, *J. Appl. Phys. (Melville, NY)* **71**, 4382 (1992).
- [34] V. Ariel, [arXiv:1205.3995](https://arxiv.org/abs/1205.3995) [physics.gen-ph].
- [35] W. Liu and E. Wang, *J. Appl. Phys. (Melville, NY)* **126**, 075706 (2019).
- [36] J. Kono, A. H. Chin, A. P. Mitchell, T. Takahashi, and H. Akiyama, *Appl. Phys. Lett.* **75**, 1119 (1999).
- [37] D. Dragoman and M. Dragoman, *Optical Characterization of Solids* (Springer, New York, 2002).